Fourier Transform approach to numerical homogenization of periodic media containing sharp insulating and superconductive cracks

Quy-Dong To, Guy Bonnet

Fourier Transform approach to numerical homogenization of periodic media containing sharp insulating and superconductive cracks

Quy-Dong To[a,*], Guy Bonnet[a]

[a]*Laboratoire MSME, Univ Gustave Eiffel, CNRS UMR 8208, F-77454 Marne-la-Vallée, France*

Abstract

In the present paper, we propose a new FFT based numerical homogenization method to compute the effective conductivity of fractured media involving insulating and superconductive cracks. The governing Lippmann Schwinger (LS) equations based on temperature jump and heat flux jump distribution localized on crack lines are formulated and the geometry of sharp cracks is described by exact expression of form factors. To solve the LS equations, the bi conjugate gradient stabilized method is used and leads to fast convergence. Numerical examples in 2D and 3D show a good accuracy when compared with standard Finite Element Method solutions.

Keywords: Fast Fourier Transform, Numerical homogenization method, Fractured media, Iteration scheme, insulating crack, superconductive crack

1. Introduction

Numerical homogenization is a special branch of computation methods devoted to the determination of overall behavior of heterogeneous materials from their constituents. Their objective is to solve the boundary value problem on a Representative Volume Element (RVE) and then obtain the

*Corresponding author. Email: quy-dong.to@univ-eiffel.fr

macroscopic relations between the averages of the local quantities. Numerical methods which have been used for this purpose can be decomposed into two main ingredients: the discretization and the resolution. The former transforms the governing equations involving the continuous quantities into discrete forms, e.g the finite difference (Lei et al., 2019), finite volume (Amraei and Fallah, 2016), finite element (Belitschko et al., 2009; Cervera et al., 2021), boundary element methods (Aliabadi, 2003) etc. for cracked and non cracked media. The latter solves the discrete equations with a solver based on a suitable algorithm e.g conjugate gradient, minimal residual iterative schemes (see e.g Saad, 2003; Barrett et al., 1994, and the references therein). Depending on the discretization schemes, solvers can be constructed based on FFT techniques, e.g spectral Galerkin (Fata and Gray, 2009; Hu et al., 2022), finite difference (Feng and S., 2020; Costa, 2022; Ren et al., 2022; Willot et al., 2014), finite element (Schneider, 2022; Zeman et al., 2017), finite volume (Nunez et al., 2012), discrete element (Calvet et al., 2022),...

Among the numerical methods, the class of Fourier Transform methods used in the present work has seen a fast development in the recent years, but with very few developments for problems involving cracks. The method is based on the formulation of Lippmann Schwinger (LS) type integral equations (Brown Jr, 1955; Kröner, 1977) involving periodic Green tensors and the iterative resolution schemes to obtain the solution. Since the Green tensors and their convolution action are generally known in frequency space, the Fast Fourier Transform is useful to switch back and forth between the physical space and the frequency space (Moulinec and Suquet, 1994; Michel et al., 1999).

Many contributions have been proposed to improve the method and to extend it to different fields of physics. Eyre and Milton (1999) proposed an accelerated scheme based on polarization basis and showed that the conver-

gence rate is significantly increased. The LS equation can be viewed as a linear equation and solved by Newton-Krylov solvers (Zeman et al., 2010; Vondřejc et al., 2014; Schneider, 2019; Kabel et al., 2014). Alternatively, the linear equations can be constructed from the variational principle at stationary state (Brisard and Dormieux, 2010). Willot et al. (2014) used a finite difference scheme leading to a modified expression of Green tensors and improving the results for infinite contrast cases. The methods can also avoid fluctuations inherent to the Fourier series. For the methods based on original Green tensors, the fluctuations near the interface can be attenuated by using smoothing filters to post process the results (Morin et al., 2021). Another method is to use composite voxels that improve significantly the quality of solutions near the interfaces (Kabel et al., 2015).

The application of FFT methods to cracks is based on previous works related to porous materials. A porous material can be considered as a special heterogeneous material with two distinct phases: the skeleton and the void. The void can be considered empty or filled with air in the usual sense which has a very small (zero) conductivity when compared with the skeleton. This is called insulating pore. In the other extreme, the void can be occupied by superconductive materials which have a very large ("infinite") conductivity with respect to the host material, e.g large water saturated pore surrounded by low porosity matrix or graphene or carbon nanotube in reinforced concrete etc. Those two cases fall into the category of infinite contrast problems which cause convergence issues to classical FFT algorithm. Furthermore, in many cases of interest, the pore geometry is reduced to a crack where the volume and thickness is equal to zero, making the problem more challenging. Among the works documented in literature, discrete Green tensors (Gasnier et al., 2018) have been used to study cracks. However, in this method, the pixel based formulation introduces a numerical thickness of the cracks equal to the voxel size and zigzag geometry and non uniform thickness when they

are not parallel to the grid axis. Another method to deal with a distribution of cracks was to use an approach based on damage mechanics (Chen et al., 2019). However, this method focuses on crack propagation and does not deal with sharp cracks. In the present paper, a FFT method dealing with cracks of zero thickness is presented. We note that the case of finite insulating pore can be treated by LS equations derived for skeleton temperature (To and Bonnet, 2020; To et al., 2021). It suggested that the method could be extended to insulating and superconductive cracks.

In the present paper, we consider fractured media involving insulating and superconductive cracks. Starting from the LS equation for porous media, we formulate the LS equations in the crack limit for temperature jump distribution (insulating crack) and flux jump distribution (superconductive crack). Such a formulation requires the description of the crack geometry via form factors, which are capable of modelling sharp cracks as polylines and polygons of discontinuity at any location in space. The governing equations are solved by a Krylov based method, specifically the bi conjugate gradient stabilized method which proves to be fast and generate accurate results, when combined with suitable post process smoothing filters. Numerical examples in 2D and 3D cases show a good agreement with a Finite Element Method solution and capture well the physics of heat transfer through cracked media.

2. Formulation and resolution method

2.1. Mathematical preliminaries

A $V-$ periodic function $\boldsymbol{u}(\boldsymbol{x})$ of cartesian coordinates $\boldsymbol{x}(x_1, x_2, x_3)$ can be expressed as Fourier series

$$\boldsymbol{u}(\boldsymbol{x}) = \sum_{\boldsymbol{\xi}} \widehat{\boldsymbol{u}}(\boldsymbol{\xi}) e^{i\boldsymbol{\xi}\boldsymbol{x}} \tag{1}$$

where $\widehat{\boldsymbol{u}}(\boldsymbol{\xi})$ is the Fourier transform of $\boldsymbol{u}(\boldsymbol{x})$:

$$\widehat{\boldsymbol{u}}(\boldsymbol{\xi}) = \mathcal{F}[\boldsymbol{u}(\boldsymbol{x})] = \frac{1}{V}\int_V \boldsymbol{u}(\boldsymbol{x}) e^{-i\boldsymbol{\xi}\boldsymbol{x}} d\boldsymbol{x}, \quad i = \sqrt{-1} \tag{2}$$

and $\boldsymbol{\xi}$ the wave vector with components ξ_1, ξ_2, ξ_3

$$\xi_k = 2\pi n_k / L_k, \quad n_k = 0, \pm 1, \pm 2, ..., \pm\infty, \quad k = 1, 2, 3 \tag{3}$$

and L_1, L_2, L_3 being the dimensions of the period V along directions x_1, x_2, x_3. Numerically, the number of wave vectors is limited by parameter N called resolution parameter satisfying

$$-N < n_k \leq N \quad k = 1, 2, 3 \tag{4}$$

The convolution product $*$ of operator $\boldsymbol{A}$ on $\boldsymbol{u}$ in physical space can be expressed as

$$\boldsymbol{A}(\boldsymbol{x}) * \boldsymbol{u}(\boldsymbol{x}) = \sum_{\boldsymbol{\xi}} \widehat{\boldsymbol{A}}(\boldsymbol{\xi}) \widehat{\boldsymbol{u}}(\boldsymbol{\xi}) e^{i\boldsymbol{\xi}\boldsymbol{x}} \tag{5}$$

and the normal product has the following form

$$\boldsymbol{A}(\boldsymbol{x})\boldsymbol{u}(\boldsymbol{x}) = \sum_{\boldsymbol{\xi}} [\widehat{\boldsymbol{A}}(\boldsymbol{\xi}) * \widehat{\boldsymbol{u}}(\boldsymbol{\xi})] e^{i\boldsymbol{\xi}\boldsymbol{x}} \tag{6}$$

with the discrete convolution product in Fourier space

$$\widehat{\boldsymbol{A}}(\boldsymbol{\xi}) * \widehat{\boldsymbol{u}}(\boldsymbol{\xi}) = \sum_{\boldsymbol{\xi}'} \boldsymbol{A}(\boldsymbol{\xi} - \boldsymbol{\xi}') \boldsymbol{u}(\boldsymbol{\xi}') \tag{7}$$

In the paper, we use a set of operators $\boldsymbol{P}$, $\boldsymbol{R}$ and S whose expressions in the Fourier space $\widehat{\boldsymbol{P}}(\boldsymbol{\xi})$, $\widehat{\boldsymbol{R}}(\boldsymbol{\xi})$ and $\widehat{S}(\boldsymbol{\xi})$ are explicit functions of wave vector $\boldsymbol{\xi}$

and the anisotropic reference conductivity $\boldsymbol{K}^r$, for example

$$\widehat{\boldsymbol{P}}(\boldsymbol{\xi}) = \frac{\boldsymbol{\xi} \otimes \boldsymbol{\xi}}{\boldsymbol{\xi}\boldsymbol{K}^r\boldsymbol{\xi}}, \quad \widehat{\boldsymbol{R}}(\boldsymbol{\xi}) = \frac{i\boldsymbol{\xi}}{\boldsymbol{\xi}\boldsymbol{K}^r\boldsymbol{\xi}}, \quad \widehat{S}(\boldsymbol{\xi}) = \frac{1}{\boldsymbol{\xi}\boldsymbol{K}^r\boldsymbol{\xi}} \tag{8}$$

and null for $\boldsymbol{\xi} = \boldsymbol{0}$

$$\widehat{\boldsymbol{P}}(\boldsymbol{0}) = \boldsymbol{0}, \quad \widehat{\boldsymbol{R}}(\boldsymbol{0}) = 0, \quad \widehat{S}(\boldsymbol{0}) = 0 \tag{9}$$

Noting that for any function φ, we have the identity

$$-\boldsymbol{R} * \boldsymbol{K}^r \nabla\varphi = \varphi - \langle\varphi\rangle \tag{10}$$

with $\langle\varphi\rangle$ being the volume average of φ.

2.2. Integral equation for the matrix material

To determine the effective conductivity of the composite material whose local conductivity $\boldsymbol{K}(\boldsymbol{x})$ is $V-$periodic function of coordinate $\boldsymbol{x}$, we need to solve the local problem using the set of equations

$$\boldsymbol{e} = -\nabla T, \quad \boldsymbol{j}(\boldsymbol{x}) = \boldsymbol{K}(\boldsymbol{x})\boldsymbol{e}(\boldsymbol{x}), \quad \text{div } \boldsymbol{j}(\boldsymbol{x}) = 0 \tag{11}$$

where $\boldsymbol{e}$ is the (minus) periodic temperature gradient and $\boldsymbol{j}$ the periodic heat flux. The effective conductivity $\boldsymbol{K}^e$ will then be obtained from relation between the average of temperature gradient $\boldsymbol{E}$ and the average flux $\boldsymbol{J}$

$$\boldsymbol{J} = \boldsymbol{K}^e\boldsymbol{E}, \quad \boldsymbol{E} = \langle\boldsymbol{e}\rangle, \quad \boldsymbol{J} = \langle\boldsymbol{j}\rangle \tag{12}$$

Since the physical temperature T is non periodic and thus not suitable for Fourier analysis, we shall use the periodic temperature term θ defined as follows

$$\theta = -T - \boldsymbol{E}\boldsymbol{x} \tag{13}$$

Let us consider the case of two phase composites: the 'matrix' (also called 'skeleton') of volume Ω, boundary Γ which has a finite and non vanishing anisotropic conductivity $\boldsymbol{K}^r$ and the 'inclusion' which is either an insulating void $\boldsymbol{K} = 0$ or superconductive $\boldsymbol{K} = k\boldsymbol{I}$ with $k = \infty$ (see Fig. 1a). The matrix is characterized by a characteristic function χ defined on V

$$\chi(\boldsymbol{x}) = 0 \quad \text{in } \Omega, \quad \chi(\boldsymbol{x}) = 1 \quad \text{in } V\backslash\Omega \tag{14}$$

Since the solution in the inclusion phase is not unique, it is natural to find the solution in the skeleton phase only with suitable boundary conditions at the interface. The periodic skeleton temperature θ_r and gradient $\boldsymbol{e}_r$ of this regular phase are related to θ and $\boldsymbol{e}$, which is a periodic continuous extension from Ω into V via the expressions

$$\theta_r = \chi\theta, \quad \boldsymbol{e}_r = \chi\boldsymbol{e} = \chi(\boldsymbol{E} + \nabla\theta) \tag{15}$$

Moreover, we have the relations

$$\boldsymbol{e}_r = \nabla\theta_r + \boldsymbol{E}\chi + (\boldsymbol{n}\delta)_\Gamma\theta, \tag{16}$$

and the identity (To and Bonnet, 2020)

$$(\boldsymbol{n}\delta)_\Gamma\theta = 2(\boldsymbol{n}\delta)_\Gamma\theta_r \tag{17}$$

Here, $\boldsymbol{n}$ is the outward normal vector (directed into the void) and δ the delta Dirac distribution on Γ. The distribution $(\boldsymbol{n}\delta)_\Gamma$ admits the Fourier transform

$$\widehat{(\boldsymbol{n}\delta)_\Gamma}(\boldsymbol{\xi}) = \frac{1}{V}\int_\Gamma \boldsymbol{n}(\boldsymbol{x})e^{-i\boldsymbol{\xi}\boldsymbol{x}}ds \tag{18}$$

The heat flux $\boldsymbol{j}$ for the whole material defined as $\boldsymbol{j} = \boldsymbol{K}^r\boldsymbol{e}_r$, is expected to be in equilibrium with the source term div $\boldsymbol{j} + s = 0$. As a result we can

write

$$\boldsymbol{R} * \boldsymbol{K}^r(\nabla\theta_r + \boldsymbol{E}\chi + (\boldsymbol{n}\delta)_\Gamma\theta) + S * s = 0 \tag{19}$$

Applying the identity (10) to the above equation, we obtain the integral equation for temperature θ_r in skeleton phase

$$\theta_r = \Theta_r + \boldsymbol{R} * \boldsymbol{K}^r(\boldsymbol{E}\chi + (\boldsymbol{n}\delta)_\Gamma\theta) + S * s \tag{20}$$

where the interior temperature θ_r is linked to the boundary value via the term $(\boldsymbol{n}\delta)_\Gamma\theta_r$. The parameter Θ_r is the average of θ_r and can be set arbitrarily. Let us define the distribution $\boldsymbol{\omega}$ on V attached to the value on Γ

$$\boldsymbol{\omega} = (\boldsymbol{n}\delta)_\Gamma\theta \tag{21}$$

To obtain $\boldsymbol{e}_r$, differentiating both sides of (20) and using the expression (16) for $\boldsymbol{e}_r$ leads to :

$$\boldsymbol{e}_r = \boldsymbol{E}\chi + \boldsymbol{\omega} - \boldsymbol{P} * \boldsymbol{K}^r(\boldsymbol{E}\chi + \boldsymbol{\omega}) + \boldsymbol{R} * s \tag{22}$$

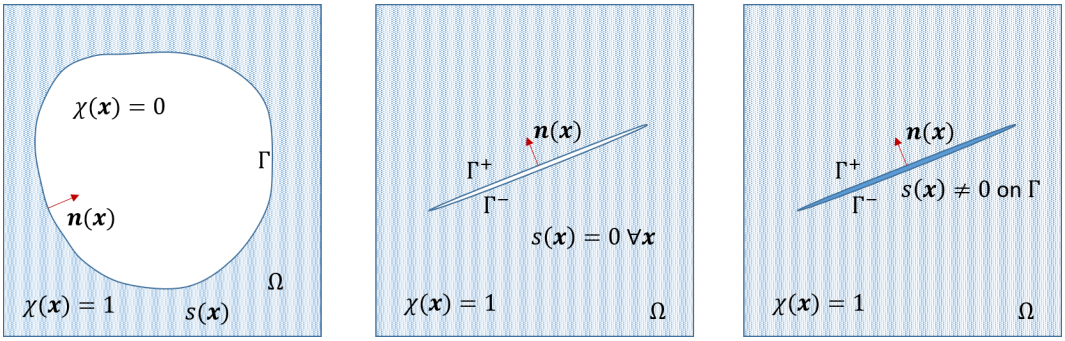

Figure 1: Sketch of the problem. Left: general porous material. Center: Media with insulating crack. Right: Media with superconductive crack.

2.2.1. Sharp insulating crack limit

In the case of a sharp crack, the boundary Γ is reduced to two faces corresponding to the upper face Γ^+ and the lower face Γ^- located at the same position Γ (see Fig. 1b). The distribution $\boldsymbol{\omega}$ now becomes

$$\boldsymbol{\omega} = -(\boldsymbol{n}\delta)_\Gamma [\![\theta]\!] \tag{23}$$

where $[\![\theta_r]\!] = \theta^+ - \theta^-$ is the temperature jump across the crack and $\boldsymbol{n}$ the normal vector of the lower face. At the crack limit, $\chi = 1 \forall \boldsymbol{x}$ and without the source term $s = 0$, all the relations for θ_r and $\boldsymbol{e}_r$ are reduced to

$$\theta_r = \Theta_r + \boldsymbol{R} * \boldsymbol{K}^r \boldsymbol{\omega}, \quad \boldsymbol{e}_r = \boldsymbol{E} + \boldsymbol{\omega} - \boldsymbol{P} * \boldsymbol{K}^r \boldsymbol{\omega} \tag{24}$$

Since the crack surface is flux free, $\boldsymbol{n}\boldsymbol{e}_r$ vanishes on both Γ^+ and Γ^-. Using the projector $\boldsymbol{n} \otimes \boldsymbol{n}$, we find that

$$(\boldsymbol{n} \otimes \boldsymbol{n}\delta)_\Gamma (\boldsymbol{P} * \boldsymbol{K}^r \boldsymbol{\omega} - \boldsymbol{\omega} - \boldsymbol{E}) = 0 \tag{25}$$

The latter can be arranged as a linear equation

$$\boldsymbol{A} \odot \boldsymbol{\omega} = \boldsymbol{b} \tag{26}$$

with the linear operators $\boldsymbol{A}\odot$ and $\boldsymbol{b}$ representing

$$\boldsymbol{A} \odot \boldsymbol{\omega} = (\boldsymbol{P} * \boldsymbol{K}^r \boldsymbol{\omega} - \boldsymbol{\omega})(\boldsymbol{n} \otimes \boldsymbol{n}\delta)_\Gamma, \quad \boldsymbol{b} = \boldsymbol{E}(\boldsymbol{n} \otimes \boldsymbol{n}\delta)_\Gamma \tag{27}$$

After resolving $\boldsymbol{\omega}$ by (26) and then the local field $\theta_r, \boldsymbol{e}_r$ by (24), the effective conductivity is given by the equation

$$\boldsymbol{E}\boldsymbol{K}^e\boldsymbol{E} = \langle \boldsymbol{e}_r \boldsymbol{K}^r \boldsymbol{e}_r \rangle \tag{28}$$

or by the average relation

$$\boldsymbol{K}^e \boldsymbol{E} = \boldsymbol{K}_r \langle \boldsymbol{e}_r \rangle \tag{29}$$

2.2.2. Sharp superconductive crack limit

We consider first the situation where the superconductive domain $V \backslash \Omega$ has non vanishing dimensions. The source term s is localized at the boundary Γ representing the heat transfer between two phases

$$s = (\boldsymbol{j}\boldsymbol{n}\delta)_\Gamma \tag{30}$$

The infinite conductivity condition implies that $\boldsymbol{e}$ vanishes in $V \backslash \Omega$ and the periodic temperature part θ must be linear in $\boldsymbol{x}$ in this domain. As a result, we have

$$\theta = C - \boldsymbol{E}\boldsymbol{x} \quad \text{on } \Gamma \tag{31}$$

Averaging θ on the boundary yields the expression of constant C

$$C = \frac{1}{|\Gamma|} \int_\Gamma (\theta + \boldsymbol{E}\boldsymbol{x}) d\boldsymbol{x} = \frac{\langle \delta_\Gamma (\theta + \boldsymbol{E}\boldsymbol{x}) \rangle}{\langle \delta_\Gamma \rangle} \tag{32}$$

At the crack limit we find that the temperature θ is continuous across Γ^+ and Γ^- and the term $(\boldsymbol{n}\delta)_{\Gamma_r}\theta$ vanishes. On the other hand, the normal heat flux $\boldsymbol{j}\boldsymbol{n}$ is discontinuous on Γ^+ and Γ^-. This is equivalent to a distribution s localized on the crack line

$$s = (\llbracket \boldsymbol{j} \rrbracket \boldsymbol{n}\delta)_\Gamma \tag{33}$$

where $\llbracket \boldsymbol{j} \rrbracket = \boldsymbol{j}^+ - \boldsymbol{j}^-$ is the normal flux jump across the crack. The equation for θ_r and $\boldsymbol{e}_r$ becomes

$$\theta_r = \Theta_r + S * s, \quad \boldsymbol{e}_r = \boldsymbol{E} + \boldsymbol{R} * s \tag{34}$$

Setting the constant $\Theta_r = 0$ (which does not affect our results), multiplying both sides of (34) with δ_Γ and using (31,32), we obtain an integral equation for the source term s

$$(S * s + \boldsymbol{E}\boldsymbol{x} - \frac{1}{\langle \delta_\Gamma \rangle} \langle \delta_\Gamma (S * s + \boldsymbol{E}\boldsymbol{x}) \rangle) \delta_\Gamma = 0 \tag{35}$$

This equation can be arranged as

$$A \star s = b \tag{36}$$

with the linear operator $A \star s$ and b being

$$A \star s = \left(S * s - \frac{\langle \delta_\Gamma S * s \rangle}{\langle \delta_\Gamma \rangle} \right) \delta_\Gamma, \quad b = \left(\frac{\langle \boldsymbol{E}\boldsymbol{x} \delta_\Gamma \rangle}{\langle \delta_\Gamma \rangle} - \boldsymbol{E}\boldsymbol{x} \right) \delta_\Gamma \tag{37}$$

After obtaining s by solving (36) and then the local field $\theta_r, \boldsymbol{e}_r$ by (34), the effective conductivity is given by the same equation as for the case of insulating crack.

2.3. Resolution by an iteration scheme

We can solve the distribution $\boldsymbol{\omega}$ for an insulating crack problem or s for a superconductive crack problem by iterations. Taking the first case as example, the simplest method would be to use the recurrence relation

$$\boldsymbol{\omega}^{(n+1)} = \boldsymbol{\omega}^{(n)} + \alpha(\boldsymbol{A} \odot \boldsymbol{\omega}^{(n)} - \boldsymbol{b}) \tag{38}$$

with α being a constant. However, it is more efficient to employ a Krylov method. Since operator $\boldsymbol{A}$ is generally non symmetric (see appendix A), we have chosen to use the biconjugate gradient stabilized (BICGSTAB) method, leading to the following algorithm:

Algorithm 1 Biconjugate gradient stabilized (BICGSTAB) iteration scheme for linear problem $\boldsymbol{A} \odot \boldsymbol{\omega} = \boldsymbol{b}$

Initialization $\boldsymbol{\omega}^{(0)} = \boldsymbol{0}$
$\boldsymbol{r}^{(0)} = \boldsymbol{b}$ and choose $\boldsymbol{r'} = \boldsymbol{r}^{(0)}$
Set $\boldsymbol{p}^{(0)} = \boldsymbol{r}^{(0)}$
for j=0,1,2,... **do**
1. $\alpha^{(j)} = (\boldsymbol{r}^{(j)}\boldsymbol{r'})/((\boldsymbol{A} \odot \boldsymbol{p}^{(j)})\boldsymbol{r'})$,
2. $\boldsymbol{s}^{(j)} = \boldsymbol{r}^{(j)} - \alpha^{(j)}(\boldsymbol{A} \odot \boldsymbol{p}^{(j)})$
if $\|\boldsymbol{s}^{(j)}\|/\|\boldsymbol{E}\delta_\Gamma\| < \varepsilon$ **then**
$\boldsymbol{\omega}^{(j+1)} = \boldsymbol{\omega}^{(j)} + \alpha^{(j)}\boldsymbol{p}^{(j)}$
BREAK
end if
3. $\gamma^{(j)} = ((\boldsymbol{A} \odot \boldsymbol{s}^{(j)})\boldsymbol{s}^{(j)})/((\boldsymbol{A} \odot \boldsymbol{s}^{(j)})(\boldsymbol{A} \odot \boldsymbol{s}^{(j)}))$
4. $\boldsymbol{\omega}^{(j+1)} = \boldsymbol{\omega}^{(j)} + \alpha^{(j)}\boldsymbol{p}^{(j)} + \gamma^{(j)}\boldsymbol{s}^{(j)}$
5. $\boldsymbol{r}^{(j+1)} = \boldsymbol{s}^{(j)} - \gamma^{(j)}(\boldsymbol{A} \odot \boldsymbol{s}^{(j)})$
if $\|\boldsymbol{r}^{(j+1)}\|/\|\boldsymbol{E}\delta_\Gamma\| < \varepsilon$ **then**
BREAK
end if
6. $\beta^{(j)} = \alpha^{(j)}/\gamma^{(j)}(\boldsymbol{r}^{(j+1)}\boldsymbol{r'})/(\boldsymbol{r}^{(j)}\boldsymbol{r'})$
7. $\boldsymbol{p}^{(j+1)} = \boldsymbol{r}^{(j+1)} + \beta^{(j)}(\boldsymbol{p}^{(j)} - \gamma^{(j)}\boldsymbol{A} \odot \boldsymbol{p}^{(j)})$
if $\|\boldsymbol{r}^{(j+1)}\boldsymbol{r'}\|/\|\boldsymbol{E}\delta_\Gamma\|^2 < \varepsilon'$ **then**
$\boldsymbol{r'} = \boldsymbol{r}^{(j+1)}$
$\boldsymbol{p}^{(j+1)} = \boldsymbol{r}^{(j+1)}$
end if
end for

Introducing a tolerance ε, the scheme is based on the residual $\boldsymbol{r}^{(j+1)}$ and stopped when

$$\frac{\|\boldsymbol{r}^{(j+1)}\|}{\|\boldsymbol{E}\delta_\Gamma\|} < \varepsilon \tag{39}$$

We note that the residual $\boldsymbol{r}^{(j+1)}$ can be viewed as a delta distribution on Γ whose strength tends to zero as the scheme converges and the error is thus chosen by normalizing the residual with $\boldsymbol{E}\delta_\Gamma$. Due to the singular nature of delta function, the norm is defined at a finite resolution N. Moreover, to

avoid divergence when $\|\boldsymbol{r}^{(j+1)}\boldsymbol{r}'\|$ is close to 0, another small control parameter ε' is also used to restart the algorithm. In all studies, we adopt the values $\varepsilon = 10^{-3}$ and $\varepsilon' = 10^{-6}$.

2.4. Form factors for sharp cracks

The form factor for crack function is given in the general formula

$$\begin{aligned}
&\widehat{(\boldsymbol{n}\otimes\boldsymbol{n}\delta)}_\Gamma(\boldsymbol{\xi}) = \frac{1}{V}\int_\Gamma \boldsymbol{n}(\boldsymbol{x})\otimes\boldsymbol{n}(\boldsymbol{x})e^{-i\boldsymbol{\xi}\boldsymbol{x}}ds \\
&\widehat{\delta}_\Gamma(\boldsymbol{\xi}) = \frac{1}{V}\int_\Gamma e^{-i\boldsymbol{\xi}\boldsymbol{x}}ds, \quad \widehat{(\boldsymbol{x}\delta)}_\Gamma(\boldsymbol{\xi}) = \frac{1}{V}\int_\Gamma \boldsymbol{x}e^{-i\boldsymbol{\xi}\boldsymbol{x}}ds
\end{aligned} \tag{40}$$

Depending on 2D and 3D problems, Γ is the collection of all discontinuity curved lines (in 2D) or surfaces (in 3D) which can be separated or interconnected. We note that general complex lines and surfaces can be approximated by polylines or polysurfaces constituted of straight and planar segments whose form factor can be evaluated more easily. For straight or planar Γ, posing $\boldsymbol{c}$ as the centroid of Γ, $\boldsymbol{x}'$ being such that $\boldsymbol{x} = \boldsymbol{c} + \boldsymbol{x}'$ and using the fact that the normal vector $\boldsymbol{n}$ is constant for those line and planar objects, we have

$$\begin{aligned}
&\widehat{(\boldsymbol{n}\otimes\boldsymbol{n}\delta)}_\Gamma(\boldsymbol{\xi}) = (\boldsymbol{n}\otimes\boldsymbol{n})\delta_\Gamma(\boldsymbol{\xi}), \quad \widehat{\delta}_\Gamma(\boldsymbol{\xi}) = \frac{1}{V}e^{-i\boldsymbol{\xi}\boldsymbol{c}}\int_\Gamma e^{-i\boldsymbol{\xi}_{||}\boldsymbol{x}'}ds \\
&\widehat{(\boldsymbol{x}\delta)}_\Gamma(\boldsymbol{\xi}) = \frac{1}{V}e^{-i\boldsymbol{\xi}\boldsymbol{c}}\left[\boldsymbol{c}\int_\Gamma e^{-i\boldsymbol{\xi}_{||}\boldsymbol{x}'}ds + \int_\Gamma \boldsymbol{x}'e^{-i\boldsymbol{\xi}_{||}\boldsymbol{x}'}ds\right]
\end{aligned} \tag{41}$$

where $\boldsymbol{\xi}_{||}$ is the projection of $\boldsymbol{\xi}$ on Γ. Additionally we have the relation

$$\widehat{(\boldsymbol{x}\delta)}_\Gamma(\boldsymbol{\xi}) = i\frac{d}{d\boldsymbol{\xi}}\widehat{\delta}_\Gamma(\boldsymbol{\xi}) \tag{42}$$

As a result, the form factor for any wave vector $\boldsymbol{\xi}$ can be deduced from the form factor for the projection of $\boldsymbol{\xi}$ on Γ. In the following, we present the exact expressions for several elementary cases of interests.

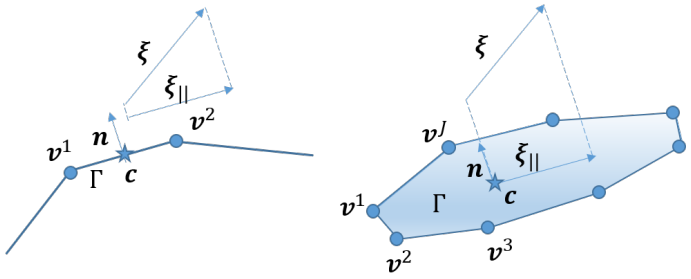

Figure 2: Geometry of Γ in 2D polyline (left) and in 3D polygon (right)

For a straight line segment in 2D problems (see Fig. 2a) connected between two vertices $\boldsymbol{v}^1$ and $\boldsymbol{v}^2$ (To et al., 2021), we have

$$\begin{aligned}
\widehat{\delta_\Gamma}(\boldsymbol{\xi}) &= \frac{2l}{V} e^{-i\boldsymbol{\xi c}} \mathrm{sinc}(\boldsymbol{\xi l}) \\
\widehat{(\boldsymbol{x}\delta)_\Gamma}(\boldsymbol{\xi}) &= \frac{2l}{V} e^{-i\boldsymbol{\xi c}} \left[\frac{i\boldsymbol{l}}{(\boldsymbol{\xi l})} [\cos(\boldsymbol{\xi l}) - \mathrm{sinc}(\boldsymbol{\xi l})] + \boldsymbol{c}\mathrm{sinc}(\boldsymbol{\xi l}) \right]
\end{aligned} \tag{43}$$

with

$$\boldsymbol{c} = \frac{1}{2}(\boldsymbol{v}^1 + \boldsymbol{v}^2), \quad \boldsymbol{l} = \frac{1}{2}(\boldsymbol{v}^2 - \boldsymbol{v}^1), \quad l = |\boldsymbol{l}| \tag{44}$$

When $\boldsymbol{\xi}_{||} = 0$ or $\boldsymbol{\xi l} = 0$, we have the identities

$$\widehat{\delta_\Gamma}(\boldsymbol{\xi}) = \frac{2l}{V} e^{-i\boldsymbol{\xi c}}, \quad \widehat{(\boldsymbol{x}\delta)_\Gamma}(\boldsymbol{\xi}) = \frac{2l}{V} e^{-i\boldsymbol{\xi c}} \boldsymbol{c} \tag{45}$$

For planar polygons in 3D problems (see Fig. 2b) with corners $\boldsymbol{v}^1, \boldsymbol{v}^2, \boldsymbol{v}^3, ..., \boldsymbol{v}^J$ in counterclockwise direction with respect to $\boldsymbol{n}$, from Wuttke (2021) and (42)

we have

$$\widehat{\delta_\Gamma}(\boldsymbol{\xi}) = \frac{2i}{V\xi_{||}^2}\cdot\sum_{j=1}^{J}\boldsymbol{\xi}_{||}(\boldsymbol{l}^j\times\boldsymbol{n})\mathrm{sinc}(\boldsymbol{\xi}\boldsymbol{l}^j)e^{-i\boldsymbol{\xi}\boldsymbol{c}^j}$$

$$\widehat{(\boldsymbol{x}\delta)_\Gamma}(\boldsymbol{\xi}) = \frac{2}{V\xi_{||}^2}\cdot\sum_{j=1}^{J}[\boldsymbol{\xi}_{||}(\boldsymbol{l}^j\times\boldsymbol{n})]e^{-i\boldsymbol{\xi}\boldsymbol{c}^j}\left[i\boldsymbol{c}^j\mathrm{sinc}(\boldsymbol{\xi}\boldsymbol{l}^j) - \frac{\boldsymbol{l}^j}{(\boldsymbol{\xi}\boldsymbol{l}^j)}[\cos(\boldsymbol{\xi}\boldsymbol{l}^j) - \mathrm{sinc}(\boldsymbol{\xi}\boldsymbol{l}^j)]\right]$$

$$+\frac{2}{V\xi_{||}^2}\cdot\sum_{j=1}^{J}\left[[\boldsymbol{\xi}_{||}(\boldsymbol{l}^j\times\boldsymbol{n})]\frac{2\boldsymbol{\xi}_{||}}{\xi_{||}^2} - (\boldsymbol{l}^j\times\boldsymbol{n})\right]\mathrm{sinc}(\boldsymbol{\xi}\boldsymbol{l}^j)e^{-i\boldsymbol{\xi}\boldsymbol{c}^j} \tag{46}$$

with

$$\boldsymbol{c}^j = \frac{1}{2}(\boldsymbol{v}^j + \boldsymbol{v}^{j-1}), \quad \boldsymbol{l}^j = \frac{1}{2}(\boldsymbol{v}^j - \boldsymbol{v}^{j-1}), \quad \boldsymbol{v}^0 \equiv \boldsymbol{v}^J \tag{47}$$

In the above expression, $\xi_{||}$ and $\boldsymbol{\xi}\boldsymbol{l}^j$ appear in the denominator and we need to examine the limit when $\boldsymbol{\xi}_{||} = 0$ and $\boldsymbol{\xi}\boldsymbol{l}^j = 0$. When $\boldsymbol{\xi}_{||} = 0$, from (41) we have

$$\widehat{\delta_\Gamma}(\boldsymbol{\xi}) = \frac{|\Gamma|}{V}e^{-i\boldsymbol{\xi}\boldsymbol{c}}, \quad \widehat{(\boldsymbol{x}\delta)_\Gamma}(\boldsymbol{\xi}) = \frac{|\Gamma|}{V}e^{-i\boldsymbol{\xi}\boldsymbol{c}}\boldsymbol{c} \tag{48}$$

and we also note that when $\boldsymbol{\xi}\boldsymbol{l}^j = 0$, the expressions with $\boldsymbol{\xi}\boldsymbol{l}^j$ in the denominator are also well defined due to the limit

$$\lim_{\boldsymbol{\xi}\boldsymbol{l}^j\to 0}\frac{\cos(\boldsymbol{\xi}\boldsymbol{l}^j) - \mathrm{sinc}(\boldsymbol{\xi}\boldsymbol{l}^j)}{(\boldsymbol{\xi}\boldsymbol{l}^j)} = 0 \tag{49}$$

The area of the polygon Γ is given by the expression

$$|\Gamma| = \frac{1}{2}\boldsymbol{n}\sum_{j=1}^{J}\boldsymbol{v}^{j-1}\times\boldsymbol{v}^j \tag{50}$$

The delta functions δ_Γ and $(\boldsymbol{x}\delta)_\Gamma$ using form factor formula can be visualized in real space. We take a quadrilateral on an inclined plane as an example and fix the resolution parameter $N = 128$, defined as the number of points

along one direction. Next, we adopt a cutting plane coinciding with the quadrilateral plane and examine the value on the plane (see Fig. 3). We can see that the colored field reflects well the properties of the delta functions. The values inside the quadrilateral are very large while the values outside are very small. For the functions δ_Γ, the values inside the quadrilateral are more or less uniform while for $x_1\delta_\Gamma$, the values change gradually depending on the coordinate x_1.

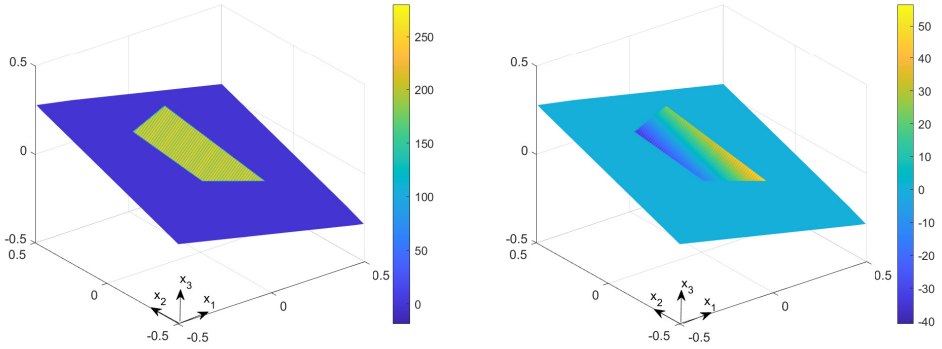

Figure 3: Delta functions δ_Γ and $(x_1\delta)_\Gamma$ in real space of a single quadrilateral crack on an inclined plane. The functions are computed in Fourier space using the form factor formulas at resolution $N = 128$ and transformed back to real space. The crack is in a unit square box V defined by $-0.5 \leq x_i \leq 0.5$ and $i = 1, 2, 3$. For the sake of clarity, the three axes x_1, x_2, x_3 of the coordinate system are shifted to the box corner.

2.5. Other numerical aspects

Due to the nature of the delta Dirac function, a fine resolution for $\widehat{(\boldsymbol{n} \otimes \boldsymbol{n}\delta)}_\Gamma(\boldsymbol{\xi})$ is required to ensure the accuracy of the solution. In most of applications, the form factor of the crack $\widehat{(\boldsymbol{n} \otimes \boldsymbol{n}\delta)}_\Gamma(\boldsymbol{\xi})$ is computed by using a double resolution, say $2N$, with respect to the base resolution N of solution $\widehat{\theta}_r(\boldsymbol{\xi}), \widehat{\boldsymbol{e}}_r(\boldsymbol{\xi})$. All the operations in the algorithm are performed in the Fourier space including the convolution, which is done using Fast Fourier Transform. The final solution of $\boldsymbol{\omega}, \theta_r, \boldsymbol{e}_r$ is obtained in Fourier space $\boldsymbol{\xi}$, then the real physical quantities are recovered by standard inverse Fourier transform.

The resolution based on Fourier series can exhibit fluctuations of the physical quantities near the crack tip. To attenuate the spurious oscillations, it is possible to adopt smoothing techniques. The traditional procedure is to modify the frequency space before doing inverse transform into physical space, e.g using low pass filters. Specifically, to smooth out the function $\varphi(\boldsymbol{x})$, instead of using direct inverse transform $\varphi(\boldsymbol{x}) = \mathcal{F}^{-1}[\widehat{\varphi}(\boldsymbol{\xi})]$, we employ a filter $\widehat{f}(\boldsymbol{\xi})$ as follows

$$\varphi(\boldsymbol{x}) \simeq \mathcal{F}^{-1}[\widehat{f}(\boldsymbol{\xi})\widehat{\varphi}(\boldsymbol{\xi})] \tag{51}$$

There are many low pass filters documented in literature which have applications in a broad range of domains related to data processing of signal and image etc...(see e.g Nixon and Aguado, 2019) As an example, the present work will use three smoothing filters as follows.

For a Gaussian filter of parameter σ_ξ, we have

$$\widehat{f}(\boldsymbol{\xi}) = e^{-|\boldsymbol{\xi}|^2/2\sigma_\xi^2} \tag{52}$$

with the typical value of σ_ξ of order N/L.

For a spline smoothing filter of parameters s, m, we have (Craven and Wahba, 1978)

$$\widehat{f}(\boldsymbol{\xi}) = \frac{1}{1 + s(\xi_1^{2m} + \xi_2^{2m} + \xi_3^{2m})} \tag{53}$$

Generally, we take $m = 1$ and $s = 10^{-5}L^{2m} - 10^{-6}L^{2m}$.

The last smoothing method is to take the local average value over a small volume, i.e square box $V_a(\boldsymbol{x})$ of dimension $2a$, centered at point $\boldsymbol{x}$ under

consideration. Using the Fourier series expression, we obtain

$$\varphi(\boldsymbol{x}) \simeq \frac{1}{8a^3}\int_{V_a(\boldsymbol{x})}\varphi(\boldsymbol{x}')d\boldsymbol{x}' = \sum_{\boldsymbol{\xi}}\widehat{\varphi}(\boldsymbol{\xi})e^{i\boldsymbol{\xi}\boldsymbol{x}}\frac{1}{8a^3}\int_{V_a(\boldsymbol{x})}e^{i\boldsymbol{\xi}(\boldsymbol{x}'-\boldsymbol{x})}d\boldsymbol{x}'$$
$$= \sum_{\boldsymbol{\xi}}\widehat{\varphi}(\boldsymbol{\xi})e^{i\boldsymbol{\xi}\boldsymbol{x}}\frac{1}{8a^3}\int_{V_a(\boldsymbol{0})}e^{i\boldsymbol{\xi}\boldsymbol{x}'}d\boldsymbol{x}' = \sum_{\boldsymbol{\xi}}\widehat{\varphi}(\boldsymbol{\xi})\widehat{f}(\boldsymbol{\xi})e^{i\boldsymbol{\xi}\boldsymbol{x}} \quad (54)$$

In this case the filter $f(\boldsymbol{\xi})$ becomes a sinc filter in frequency space as follows

$$\widehat{f}(\boldsymbol{\xi}) = \frac{1}{8a^3}\int_{-a}^{a}\int_{-a}^{a}\int_{-a}^{a}e^{i\boldsymbol{\xi}\boldsymbol{x}'}d\boldsymbol{x}' = \mathrm{sinc}(\xi_1 a)\mathrm{sinc}(\xi_2 a)\mathrm{sinc}(\xi_3 a) \quad (55)$$

The typical value of a is $a = L/2N$ which is the size of the pixel.

All smoothing filters have the properties that they attribute decreasing weights for high frequencies which are responsible for the strong fluctuation. Using very large value of σ_ξ and very small value of s corresponds to an unsmoothed solution.

As suggested by Morin et al. (2021), a smoothing filter can be applied in two situations:
- to post process the results after solving the governing equations
- to pre process the microstructure before solving the governing equations
The latter in fact, is equivalent to bringing a smooth change of materials' properties at the interface. In our method, the filter can be applied to smooth the delta functions, i.e $\delta_\Gamma(\boldsymbol{\xi})$ and $(\boldsymbol{n}\otimes\boldsymbol{n}\delta)_\Gamma(\boldsymbol{\xi})$.

3. Computation examples

3.1. Single crack problems

In this section we shall apply the FFT method developed previously to single insulating or superconductive crack problems. Those cracks are straight lines of discontinuity whose geometrical form factor has been given

in Section 2.4. The performance and the accuracy of the method will be assessed by comparison with the standard solution obtained by Finite Element Method (FEM) with details provided in Appendix B.

In the first problem, we study a 2D geometry where a single insulating crack is embedded in a matrix of conductivity $k_r = 1$ [W/mK] or $\boldsymbol{K}^r = k_r \boldsymbol{I}$. The crack has a length of $l = 0.6$ [m], is parallel to axis x_1 and located at the center of a unit volume V with dimensions $L_1 = L_2 = 1$ [m]. The prescribed macroscopic flux is directed along direction x_2, $\boldsymbol{E} = \boldsymbol{i}_2$ [K/m]. For the resolution $N = 256$ and tolerance $\varepsilon = 0.001$, the scheme stops at 21 iterations and yields the effective conductivity along direction 2 equal to $K_2^e = 0.744$ [W/mK] which is in good agreement with FEM 0.748 [W/mK]. Qualitatively looking at the solution fields in Fig. 4, we recover the discontinuity of temperature at the crack line and a high value of temperature gradient near the crack tip as expected.

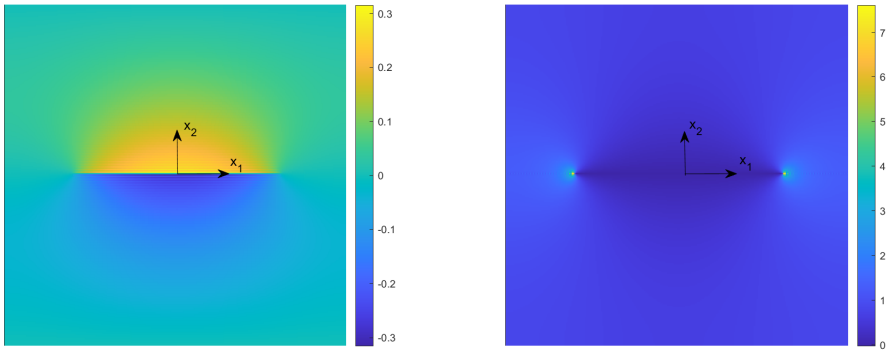

Figure 4: Periodic temperature field θ_r [K] (left) and temperature gradient field e_{r2} [K/m] (right) for the case of insulating crack. The macroscopic gradient is along direction 2, i.e $\boldsymbol{E} = \boldsymbol{i}_2$ [K/m]

To investigate the accuracy of the local field, we plot the temperature and temperature gradient on axes x_1 and x_2 and compare with FEM. Figure 5

shows an excellent agreement between the FFT and FEM solution concerning the temperature θ_r and e_{r2} on the axis x_2. Regarding e_{r1} on axis x_1, the agreement is also globally good. While the solution far from the crack tip agrees well with the FEM solution, oscillation near the crack tip is observed in the unsmoothed FFT solution. Such a fluctuation is associated to Gibbs phenomenon and can be attenuated by a smoothing filter (sinc filter for example) and thus extend further the agreement near the crack tip zone.

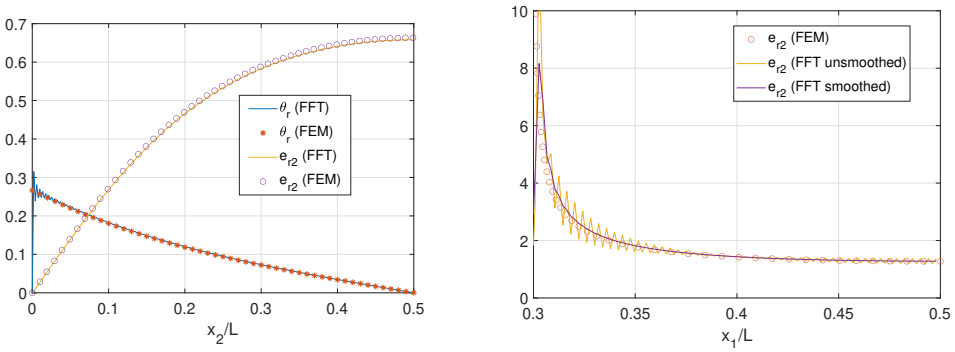

Figure 5: Periodic temperature θ_r [K] and temperature gradient e_{r2} [K/m] profile on axis x_2 (left) and temperature gradient e_{r2} [K/m] on axis x_1 for 2D slit crack (right). The smoothed results for temperature gradient e_{r2} [K/m] on axis x_1 are obtained by sinc filter post process (right).

Next, the superconductive crack of the same dimension will be considered. The prescribed macroscopic flux is directed along direction x_1, $\boldsymbol{E} = \boldsymbol{i}_1$ [K/m]. The algorithm converges after 14 iterations. The effective conductivity along x_1 is $K_1^e = 1.34$ [W/mK], which is in good agreement with 1.35 [W/mK] by FEM. In contrast to the case of insulating crack, we obtain a continuous temperature field θ_r with higher values of $|\theta_r|$ near the crack tips (see Fig. 6). In terms of temperature gradient e_{r1}, we find very high values near the crack tip as expected.

The comparison between FFT and FEM also shows an excellent agreement

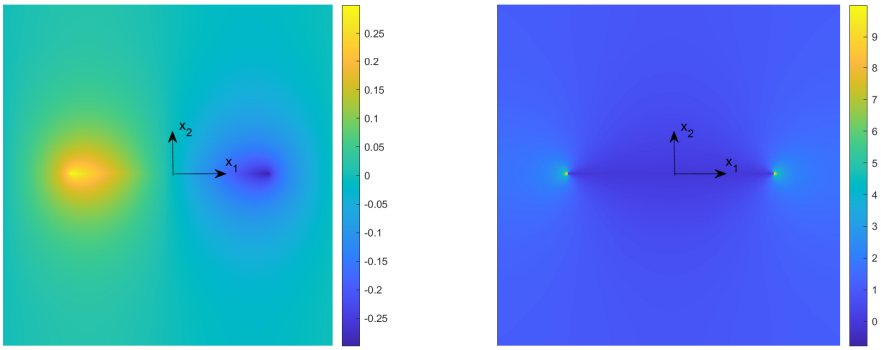

Figure 6: Periodic temperature field θ_r [K] (left) and temperature gradient field e_{r1} [K/m] (right) for the case of superconductive crack. The macroscopic gradient is along direction 1, i.e $\boldsymbol{E} = \boldsymbol{i}_1$ [K/m].

between the two methods (see Fig. 7). The temperature θ_r on axis x_1 is linear on the superconductive crack and tends to 0 at the periodic boundary. Like in the case of insulating crack, the solution has a good accuracy, except that now the oscillation of e_{r1} is found in a large part of the curve. The smoothed values are in very good agreement with the FEM solution.

We note that although the FFT method obtains the effective property of the cracked material with a good accuracy, to reproduce the local singularity $r^{-0.5}$ near the crack tip, it is necessary to adopt a fine mesh or high resolution N. This is due to the fact that the method is based on a regular grid in physical space. The log-log plot in figure 8 shows what happens near the crack tip when N increases and from the slope, we find a power relation between r and e_{r1}, e_{r2} at small r. Specifically, at highest N value $N = 1024$, we have $e_{r1} \sim r^{\alpha}$ with $\alpha = -0.51$ for insulating cracks $\alpha = -0.49$ for superconductive crack, which is close to the value $\alpha = -0.5$ predicted by the theory.

As shown above, for both types of cracks, the temperature gradient fields exhibit a fluctuation near the crack tip where theoretically the singularity of

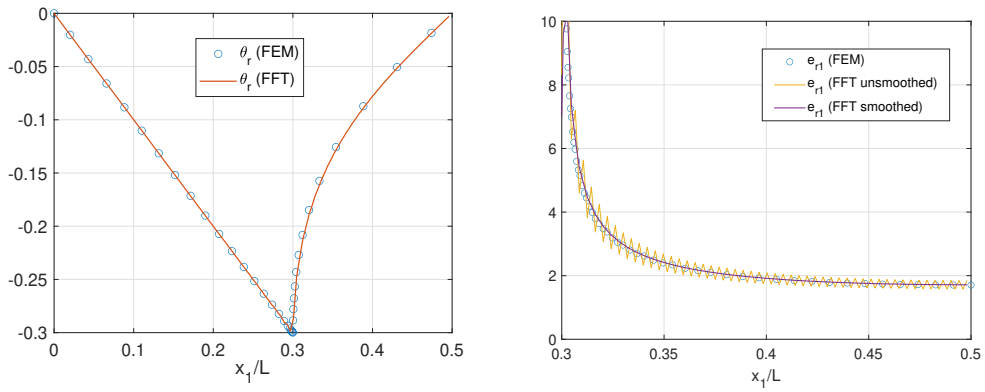

Figure 7: Periodic temperature θ_r [K] (left) and temperature gradient e_{r1} [K/m] profile on axis x_1 (right) for 2D superconductive crack. The smoothed results are obtained by sinc filter post process.

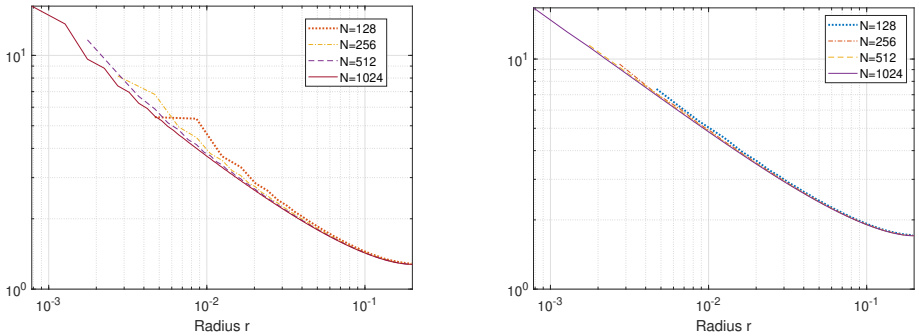

Figure 8: Temperature gradient (smoothed with sinc filter) as a function of distance to the crack tip r [m]. Left: $e_{r2}(r)$ [K/m] for insulating crack. Right: $e_{r1}(r)$ [K/m] for superconductive crack

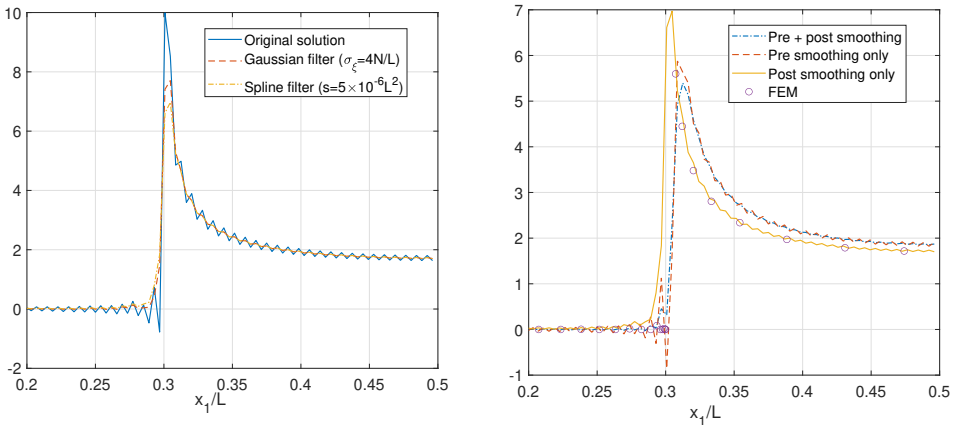

Figure 9: The temperature gradient e_{r1} [K/m] profile on axis x_1 for 2D superconductive crack. Left: Effect of post process smoothing filters. Right: Comparison of pre and post smoothing (spline smoothing with the same parameters) and FEM solution

type $r^{-0.5}$ is present. Such spurious oscillations can be attenuated using low pass filters introduced earlier in Section 2.5. In the above example, we have used sinc filter. Let us now examine the Gaussian filter and the spline filter. Taking the case of superconductive crack as an example, Figure 9a shows that both Gaussian and spline filters with suitable parameters ($\sigma_\xi = 4N/L$ for Gaussian filter and $s = 5 \times 10^{-6}L^2$ for spline filter) successfully reduce the fluctuation of the solution near the crack tip, while almost unmodifying the far field solution. By examining the effect of pre and post smoothing on the obtained solution, we use spline smoothing with the same parameters $s = 5 \times 10^{-6}L^2$ (see Fig. 9b). We find that the pre smoothing does provide smoother solution but affects the accuracy of the solution and the performance (more iterations are required). It is because pre smoothing modifies the delta functions by smearing out the sharp crack and thus the governing equations. In this case, the post smoothing is clearly better, agreeing well with the FEM results.

3.2. Multiple isolated and intersecting cracks

In this section, we investigate 2D media containing multiple cracks. In this example, 12 cracks have the same length 0.3 but random positions and orientations. Like in the previous examples, the algorithm for insulating cracks and superconductive cracks cases converge fast with 57 and 31 iterations respectively.

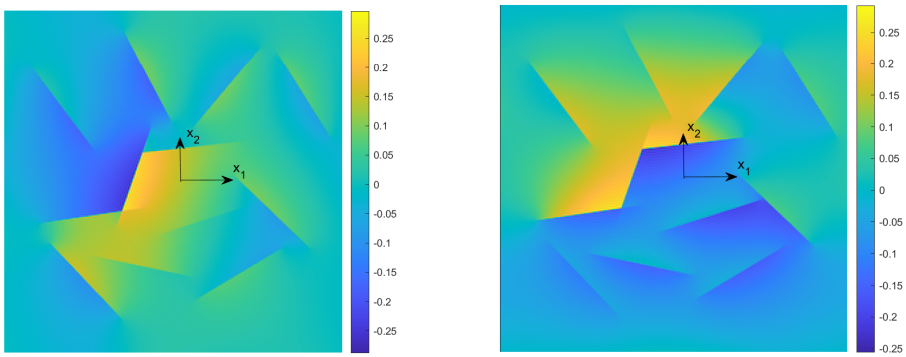

Figure 10: Periodic temperature field θ_r for cracked media: insulating crack media subject to $\boldsymbol{E} = \boldsymbol{i}_1$ [K/m] (left) and $\boldsymbol{E} = \boldsymbol{i}_2$ [K/m] (right).

Let us look first at the insulating crack case (see Fig. 10). From the color field, we can observe a temperature jump across each crack corresponding to the opposite direction of $\boldsymbol{E}$, i.e higher temperature on the right and lower temperature on the left for $\boldsymbol{E} = \boldsymbol{i}_2$ [K/m], and higher temperature at the top and lower temperature at the bottom for $\boldsymbol{E} = \boldsymbol{i}_1$ [K/m]. As a global behavior, the three intersecting insulating cracks in the middle form a large composite crack blocking the flux along the direction of macroscopic gradient $\boldsymbol{E}$ and generating the most significant temperature jump.

Regarding the case of superconductive cracks (see Fig. 11), the temperature is shown as before to be continuous with a gradual change along the

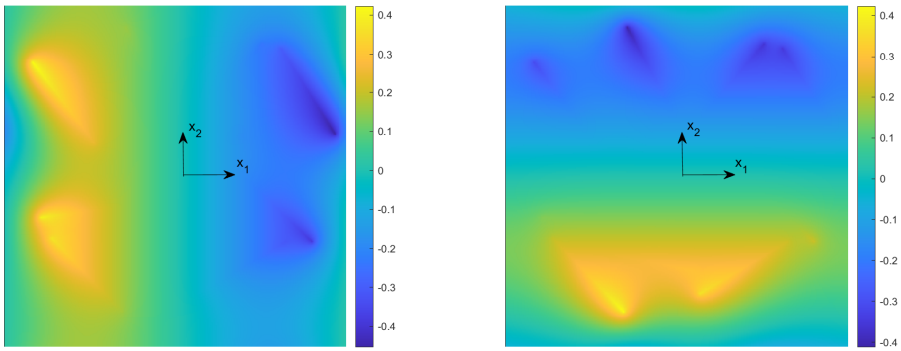

Figure 11: Periodic temperature field θ_r [K] for cracked media: superconductive crack subject to $\boldsymbol{E} = \boldsymbol{i}_1$ [K/m] (left) and $\boldsymbol{E} = \boldsymbol{i}_2$ [K/m] (right).

direction of the macroscopic gradient $\boldsymbol{E}$, especially for areas in the middle of the sample. We note that the periodic temperature θ_r in each crack is $\theta_r = C - \boldsymbol{E}\boldsymbol{x}$. As a result, θ_r concentration is pronounced at the cracks at two ends of the sample and affects the temperature distribution around these locations.

Until now, we have only considered 2D problems involving cracks as lines of discontinuity. In the final example, we shall demonstrate the performance of the method in the 3D case with cracks as surfaces of discontinuity. A 3D crack system composed of 4 quadrilateral cracks is generated for the study. All the cracks have the same shape but random locations and orientations. They intersect and form a large complex crack as seen in Fig 12. The analytical form factors for planar polygonal shape δ_Γ and $\boldsymbol{x}\delta_\Gamma$ are used. The sample of insulating cracks is subject to macroscopic gradient $\boldsymbol{E} = \boldsymbol{i}_3$ [K/m] and the case of superconductive crack $\boldsymbol{E} = \boldsymbol{i}_1$ [K/m]. Both examples converge after 50 iterations. Due to the complex solution field, we shall extract the solution on the plane of the quadrilateral in the middle that intersects the three remaining cracks. The physical temperature $T = -\theta_r - \boldsymbol{E}\boldsymbol{x}$ instead of

the periodic temperature θ_r will be plotted in the graphics.

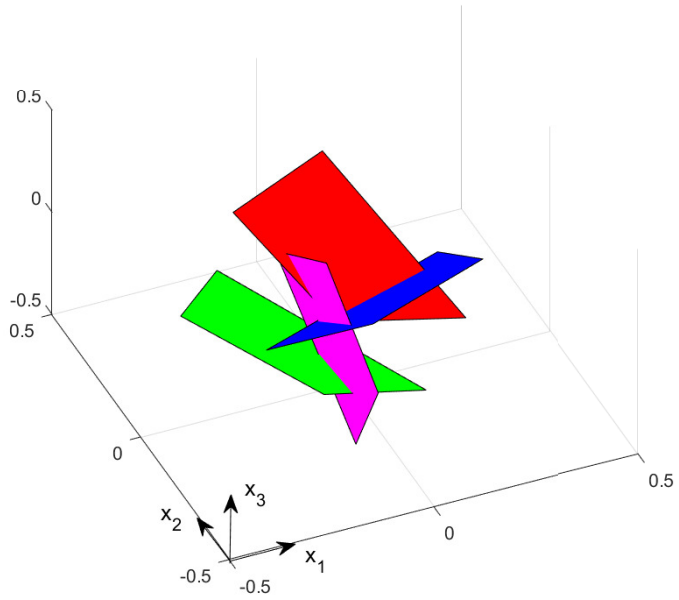

Figure 12: System of four intersecting quadrilateral cracks of the same shape but with different locations and orientations. For the sake of clarity, the three axes x_1, x_2, x_3 of the coordinate system are shifted to the box corner.

Again for the case of insulating cracks (see Fig. 13), we observe a discontinuity of temperature T across the intersection of 3 out-of-plane cracks. We also note that the temperature discontinuity of the in-plane crack is along the normal direction and can not be seen in the cut. Despite the discontinuity, the variation of T in the plane reflects well the directions of $\boldsymbol{E}$, i.e higher temperature from low altitude x_3 and lower temperature from high altitude x_3.

For the case of superconductive cracks (see Fig. 14), the temperature continuity is everywhere. Due to the connectivity, the temperature of the in-plane

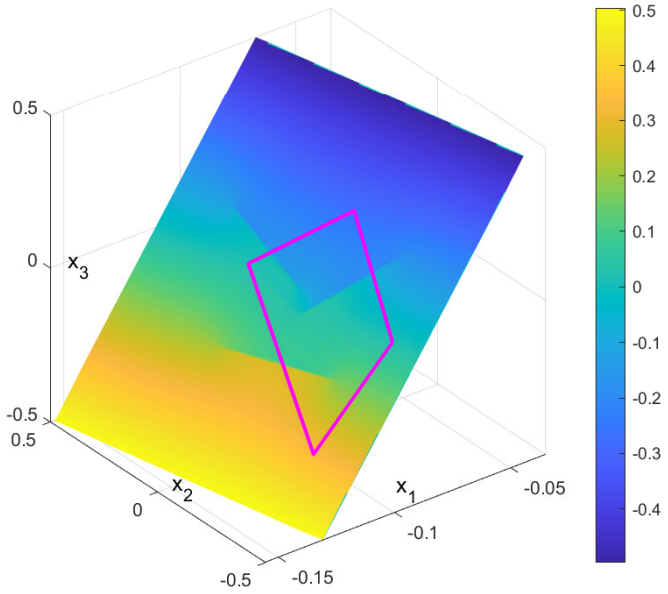

Figure 13: Physical temperature field $T = -\boldsymbol{E}\boldsymbol{x} - \theta_r$ [K] on the plane of a quadrilateral insulating crack. The prescribed macroscopic gradient is $\boldsymbol{E} = \boldsymbol{i}_3$ [K/m].

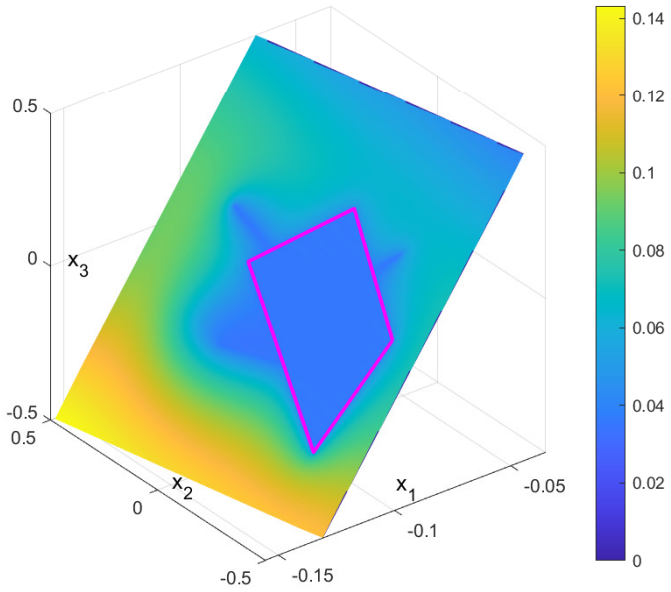

Figure 14: Physical temperature field $T = -\boldsymbol{E}\boldsymbol{x} - \theta_r$ [K] on the plane of a quadrilateral. The prescribed macroscopic gradient is $\boldsymbol{E} = \boldsymbol{i}_1$ [K/m]

crack is uniform $T = cst$ and the same as the three out-of-plane cracks. The global variation of T also agrees with the direction of $\boldsymbol{E}$ along x_1.

4. Concluding remarks

In this paper, we have presented a FFT based method to solve conductive fractured problems with sharp insulating or superconductive cracks. Although these problems are encountered frequently in engineering applications, they pose two major difficulties to the classical FFT method: infinite contrast ratio and zero dimension geometry associated to discontinuities and singularities of physical quantities. Those difficulties cause convergence issues and affect the accuracy of the previous pixel based techniques.

Based on previous works for porous material (To and Bonnet, 2020; To et al., 2021), the new LS governing equations can be derived when the pore tends to the crack limit. In this case, the temperature jump and the heat flux jump are unknown and can be solved in the new formulation. They are described by using specific delta functions localized on the crack lines and surfaces whose form factors are known analytically. Finally, the Krylov space iteration method is employed to obtain the solutions and proves to be fast and accurate. The method described in this work can be easily extended to deal with cracks in elastic domains. This will be studied in a future work.

Appendix A. Symmetry study of operator $\boldsymbol{A}$

By definition, operator $\boldsymbol{A}\odot$ is symmetric if the following scalar product equality holds for all $\boldsymbol{u}, \boldsymbol{v}$

$$\frac{1}{V}\int_V (\boldsymbol{A}\odot\boldsymbol{u})\boldsymbol{v}d\boldsymbol{x} = \frac{1}{V}\int_V (\boldsymbol{A}\odot\boldsymbol{v})\boldsymbol{u}d\boldsymbol{x}, \quad \forall \boldsymbol{u}, \boldsymbol{v} \tag{A.1}$$

or equivalently in Fourier space

$$\sum_{\boldsymbol{\xi}} \widehat{(\boldsymbol{A}\odot\boldsymbol{u})}(\boldsymbol{\xi})\widehat{\boldsymbol{v}}(-\boldsymbol{\xi}) = \sum_{\boldsymbol{\xi}} \widehat{(\boldsymbol{A}\odot\boldsymbol{v})}(\boldsymbol{\xi})\widehat{\boldsymbol{u}}(-\boldsymbol{\xi}) \tag{A.2}$$

We are also limited to the special case where $\boldsymbol{K}^r$ is isotropic and $\boldsymbol{K}^r = k^r\boldsymbol{I}$ and $\boldsymbol{P}*\boldsymbol{K}^r$ and S can be simplified as $\boldsymbol{P}'$ and S' with expressions

$$\widehat{\boldsymbol{P}'}(\boldsymbol{\xi}) = \frac{\boldsymbol{\xi}\otimes\boldsymbol{\xi}}{\xi^2}, \quad \widehat{\boldsymbol{S}'}(\boldsymbol{\xi}) = \frac{1}{k^r\xi^2} \tag{A.3}$$

Furthermore, we consider that Γ is a straight line so that the normal vector $\boldsymbol{n}$ is constant or $(\boldsymbol{n}\otimes\boldsymbol{n}\delta)_\Gamma = \boldsymbol{n}\otimes\boldsymbol{n}\delta_\Gamma$.

In the case of insulating crack, operator $\boldsymbol{A}\odot$ has the form

$$\boldsymbol{A}\odot\boldsymbol{\omega} = (\boldsymbol{P}'*\boldsymbol{\omega}-\boldsymbol{\omega})(\boldsymbol{n}\otimes\boldsymbol{n}\delta)_\Gamma \tag{A.4}$$

From the definition, it is clear that the action of $(\boldsymbol{n}\otimes\boldsymbol{n}\delta)_\Gamma$ is symmetric. However, we shall show that the product $(\boldsymbol{n}\otimes\boldsymbol{n}\delta)_\Gamma\boldsymbol{P}'$ is not symmetric, which makes $\boldsymbol{A}\odot$ non symmetric. Indeed, let us take the two fields $\boldsymbol{u} = \boldsymbol{u}_0 e^{i\boldsymbol{\xi}_0\boldsymbol{x}}$ and $\boldsymbol{v} = \boldsymbol{v}_0 e^{i\boldsymbol{\xi}_0'\boldsymbol{x}}$ as two test functions with $\boldsymbol{u}_0$ and $\boldsymbol{v}_0$ being two constant vectors and $\boldsymbol{\xi}_0$ and $\boldsymbol{\xi}_0'$ two constant wave vectors. We find that $\boldsymbol{P}'*\boldsymbol{u} = \widehat{\boldsymbol{P}'}(\boldsymbol{\xi}_0)\boldsymbol{u}_0 e^{i\boldsymbol{\xi}_0\boldsymbol{x}}$ and thus

$$\begin{aligned}&\frac{1}{V}\int_V [(\boldsymbol{n}\otimes\boldsymbol{n}\delta)_\Gamma\boldsymbol{P}'*\boldsymbol{u}]\boldsymbol{v}d\boldsymbol{x} = (\boldsymbol{n}\otimes\boldsymbol{n})(\widehat{\boldsymbol{P}'}(\boldsymbol{\xi}_0)\boldsymbol{u}_0)\boldsymbol{v}_0\frac{1}{V}\int_\Gamma e^{i(\boldsymbol{\xi}_0+\boldsymbol{\xi}_0')}d\boldsymbol{x}\\ &= (\boldsymbol{n}\otimes\boldsymbol{n})(\widehat{\boldsymbol{P}'}(\boldsymbol{\xi}_0)\boldsymbol{u}_0)\boldsymbol{v}_0\widehat{\delta}_\Gamma(-\boldsymbol{\xi}_0-\boldsymbol{\xi}_0')\end{aligned} \tag{A.5}$$

Analogously, we have $\boldsymbol{P}'*\boldsymbol{v} = \widehat{\boldsymbol{P}'}(\boldsymbol{\xi}_0')\boldsymbol{v}_0 e^{i\boldsymbol{\xi}_0'\boldsymbol{x}}$ and

$$\frac{1}{V}\int_V [(\boldsymbol{n}\otimes\boldsymbol{n}\delta)_\Gamma\boldsymbol{P}'*\boldsymbol{v}]\boldsymbol{u}d\boldsymbol{x} = (\boldsymbol{n}\otimes\boldsymbol{n})(\widehat{\boldsymbol{P}'}(\boldsymbol{\xi}_0')\boldsymbol{v}_0)\boldsymbol{u}_0\widehat{\delta}_\Gamma(-\boldsymbol{\xi}_0-\boldsymbol{\xi}_0') \tag{A.6}$$

Since the two terms $\widehat{\boldsymbol{P}'}(\boldsymbol{\xi}_0)$ and $\widehat{\boldsymbol{P}'}(\boldsymbol{\xi}_0')$ are generally different for different wave vectors $\boldsymbol{\xi}_0'$ and $\boldsymbol{\xi}_0$, (A.5) is different from (A.6), which confirms that $\boldsymbol{A}$ is non symmetric.

For the case of superconductive crack, operator $A\star$ has the form

$$A \star s = \left(S * s - \frac{\langle \delta_\Gamma S * s \rangle}{\langle \delta_\Gamma \rangle} \right) \delta_\Gamma \tag{A.7}$$

Again, to prove that $A\star$ is non symmetric, we adopt the same strategy as before and consider two trial functions $u = u_0 e^{i\boldsymbol{\xi}_0 \boldsymbol{x}}$ and $v = v_0 e^{i\boldsymbol{\xi}_0' \boldsymbol{x}}$. Thus, we have

$$S * u = \widehat{S}(\boldsymbol{\xi}_0) u_0 e^{i\boldsymbol{\xi}_0 \boldsymbol{x}}, \quad S * v = \widehat{S}(\boldsymbol{\xi}_0') v_0 e^{i\boldsymbol{\xi}_0' \boldsymbol{x}} \tag{A.8}$$

The scalar product involving $A \star u$ and v becomes

$$\frac{1}{V} \int_V (A \star u) v d\boldsymbol{x} = \widehat{S}(\boldsymbol{\xi}_0) u_0 v_0 [\delta_\Gamma(-\boldsymbol{\xi}_0 - \boldsymbol{\xi}_0') - \frac{1}{\langle \delta_\Gamma \rangle} \delta_\Gamma(-\boldsymbol{\xi}_0) \delta_\Gamma(-\boldsymbol{\xi}_0')] \tag{A.9}$$

Comparing with the similar expression for the scalar product involving $A \star v$ and u

$$\frac{1}{V} \int_V (A \star v) u d\boldsymbol{x} = \widehat{S}(\boldsymbol{\xi}_0') u_0 v_0 [\delta_\Gamma(-\boldsymbol{\xi}_0 - \boldsymbol{\xi}_0') - \frac{1}{\langle \delta_\Gamma \rangle} \delta_\Gamma(-\boldsymbol{\xi}_0) \delta_\Gamma(-\boldsymbol{\xi}_0')] \tag{A.10}$$

we find that it is sufficient to choose two different wave vectors $\boldsymbol{\xi}_0$ and $\boldsymbol{\xi}_0'$ to obtain the two different scalar products. As a result, we can confirm that $A\star$ is non symmetric.

Appendix B. Information on the FEM model

The crack line is located at the center of the unit cell of size 1 [m] with the length of 0.6 [m] on axis x_1. Due to the symmetry of the problem, only 1/4 of the model limited by the inequality $0 \leq x_1, x_2 \leq 0.5$ [m] and $x_2 = 0$, $0 \leq x_1 \leq 0.3$ [m] for the crack line is studied with suitable boundary conditions. Specifically, we have

- Insulating crack with $\boldsymbol{E} = \boldsymbol{i}_2$ [K/m]: zero normal flux $j_n = 0$ [W/m^2] on the axis of symmetry x_2 and the right boundary parallel to x_2 and on the crack line. Zero temperature $T = 0$ [K] prescribed on the axis of symmetry x_1 (except the crack line) and $T = -0.5$ [K] on the upper boundary.
- Superconductive crack with $\boldsymbol{E} = \boldsymbol{i}_1$ [K/m]: zero normal flux $j_n = 0$ [W/m^2] on the axis of symmetry x_1 (except the crack line) and the upper boundary parallel to x_1, zero temperature $T = 0$ [K] prescribed on the crack line, $T = -0.5$ [K] on the right boundary.

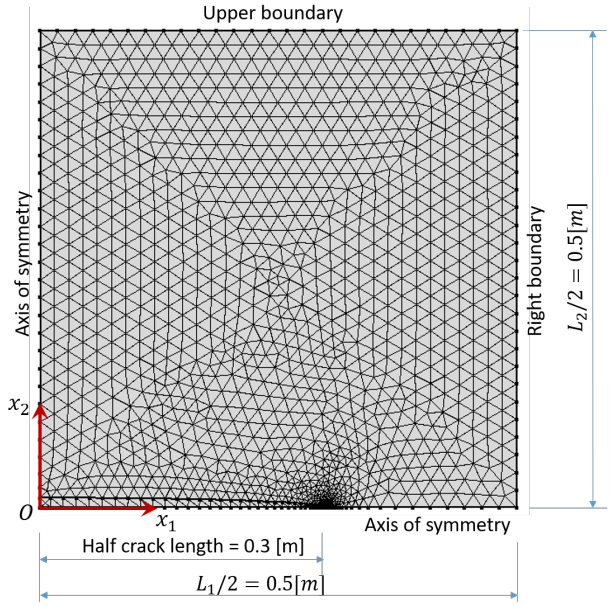

Figure B.15: Finite Element mesh of the model

Figure B.15 shows a fine mesh of the FEM model containing 2614 linear triangular elements. The commercial code COMSOL is used for the simulation.

References

Aliabadi, M., 2003. Boundary element methods in linear elastic fracture mechanics. Comprehensive structural integrity 3, 89–125.

Amraei, A., Fallah, N., 2016. A development in the finite volume method for the crack growth analysis without global remeshing. Int. J. Eng. 29, 898–908.

Barrett, R., Berry, M., Chan, T.F., Demmel, J., Donato, J., Dongarra, J., Eijkhout, V., Pozo, R., Romine, C., Van der Vorst, H., 1994. Templates for the solution of linear systems: building blocks for iterative methods. SIAM.

Belitschko, T., Gracie, R., Ventura, G., 2009. A review of extended/generalized finite element methods for material modeling. Model. Simul. Mat. Sci. Eng. 17, 043001.

Brisard, S., Dormieux, L., 2010. FFT-based methods for the mechanics of composites: A general variational framework. Comput. Mater. Sci. 49, 663–671.

Brown Jr, W.F., 1955. Solid mixture permittivities. J. Chem. Phys. 23, 1514–1517.

Calvet, T., Vanson, J., Masson, R., 2022. A DEM/FFT approach to simulate the effective thermal conductivity of granular media. Int. J. Therm. Sci. 172, 107339.

Cervera, M., Barbat, G., Chiumenti, M., Wu, J., 2021. A comparative review of xfem, mixed fem and phase-field models for quasi-brittle cracking. Arch. Comput. Methods Eng. 2, 1009–1093.

Chen, Y., Vasyukov, D., Gelebart, L., Park, C., 2019. A FFT solver for variational phase-field modeling of brittle fracture. Comput. Methods Appl. Mech. Eng.349 (2019) 167–190 349, 167–190.

Costa, P., 2022. A fft-accelerated multi-block finite-difference solver for massively parallel simulations of incompressible flows. Comput. Phys. Commun. 271, 108194.

Craven, P., Wahba, G., 1978. Smoothing noisy data with spline functions. Numerische mathematik 31, 377–403.

Eyre, D.J., Milton, G.W., 1999. A fast numerical scheme for computing the response of composites using grid refinement. Eur. Phys. J. Appl. Phys. 6, 41–47.

Fata, S., Gray, L., 2009. A fast spectral galerkin method for hypersingular boundary integral equations in potential theory. Comput. Mech. 44, 263–271.

Feng, H., S., Z., 2020. A fourth order finite difference method for solving elliptic interface problems with the fft acceleration. J. Comput. Phys. 419, 109677.

Gasnier, J.B., Willot, F., Trumel, H., Jeulin, D., Besson, J., 2018. Thermoelastic properties of microcracked polycrystals. part I: Adequacy of Fourier-based methods for cracked elastic bodies. Int. J. Solids Struct. 155, 248–256.

Hu, J., Huang, X., Shan, J., Yand, H., 2022. A fast petrov–galerkin spectral method for the multidimensional boltzmann equation using mapped chebyshev functions. SIAM J. Sci. Comput. 44, A1497–A1524.

Kabel, M., Böhlke, T., Schneider, M., 2014. Efficient fixed point and Newton–Krylov solvers for FFT-based homogenization of elasticity at large deformations. Comput. Mech. 54, 1497–1514.

Kabel, M., Merkert, D., Schneider, M., 2015. Use of composite voxels in FFT-based homogenization. Comput. Meth. Appl. Mech. Eng 294, 168–188.

Kröner, E., 1977. Bounds for effective elastic moduli of disordered materials. J. Mech. Phys. Solids 25, 137–155.

Lei, J., Xu, Y., Gu, Y., C.M., F., 2019. The generalized finite difference method for in-plane crack problems. Eng. Anal. Bound. Elem. 98, 147–156.

Michel, J., Moulinec, H., Suquet, P., 1999. Effective properties of composite materials with periodic microstructure: a computational approach. Comput. Method Appl. Mech. Eng. 172, 109–143.

Morin, L., Brenner, R., Derrien, K., Dorhmi, K., 2021. Periodic smoothing splines for FFT-based solvers. Comput. Methods Appl. Mech. Eng. 373, 113549.

Moulinec, H., Suquet, P., 1994. A fast numerical method for computing the linear and nonlinear mechanical properties of composites. C. R. Acad. Sci 318, 1417–1423.

Nixon, M., Aguado, A., 2019. Feature extraction and image processing for computer vision. Academic press.

Nunez, J., Ramos, E., Lopez, J., 2012. A mixed fourier–galerkin–finite-volume method to solve the fluid dynamics equations in cylindrical geometries. Fluid Dyn. Res. 44, 031414.

Ren, Y., Feng, H., Zhao, S., 2022. A fft accelerated high order finite difference method for elliptic boundary value problems over irregular domains. J. Comput. Phys. 448, 110762.

Saad, Y., 2003. Iterative methods for sparse linear systems. SIAM.

Schneider, M., 2019. On the Barzilai-Borwein basic scheme in FFT-based computational homogenization. Int. J. Numer. Meth. Eng. , 482–494.

Schneider, M., 2022. Voxel-based finite elements with hourglass control in fast fourier transform-based computational homogenization. Int. J. Num. Meth. Eng. doi:10.1002/nme.7114.

To, Q.D., Bonnet, G., 2020. FFT based numerical homogenization method for porous conductive materials. Comput. Meth. Appl.Mech. Eng. 368, 113160.

To, Q.D., Bonnet, G., Nguyen, T.T., 2021. Fourier transform approach to non periodic boundary value problems in porous conductive media. Int. J. Numer. Methods Eng. 122, 4864–4885.

Vondřejc, J., Zeman, J., Marek, I., 2014. An FFT-based Galerkin method for homogenization of periodic media. Comput. Math. Appl. 68, 156–173.

Willot, F., Abdallah, B., Pellegrini, Y.P., 2014. Fourier-based schemes with modified Green operator for computing the electrical response of heterogeneous media with accurate local fields. Int. J. Numer. Meth. Eng. 98, 518–533.

Wuttke, J., 2021. Numerically stable form factor of any polygon and polyhedron. J. Appl. Crystallogr. 54, 580–587.

Zeman, J., De Geus, T., Vondrejc, J., Peerlings, H., Geers, M., 2017. A finite element perspective on nonlinear FFT-based micromechanical simulations. Int. J. Num. Meth. Eng. 111, 903–926.

Zeman, J., Vondrejc, J., Novak, J., Marek, I., 2010. Accelerating a FFT-based solver for numerical homogenization of periodic media by conjugate gradients. J. Comput. Phys , 8065–8071.